JACS Au
AN OPEN ACCESS JOURNAL OF THE AMERICAN CHEMICAL SOCIETY

pubs.acs.org/jacsau

Article

Cation Overcrowding Effect on the Oxygen Evolution Reaction

Jun Huang,* Mengru Li, Mohammad J. Eslamibidgoli, Michael Eikerling, and Axel Groß

Cite This: *JACS Au* 2021, 1, 1752−1765

Read Online

ACCESS | Metrics & More | Article Recommendations | Supporting Information

ABSTRACT: The influence of electrolyte ions on the catalytic activity of electrode/electrolyte interfaces is a controversial topic for many electrocatalytic reactions. Herein, we focus on an effect that is usually neglected, namely, how the local reaction conditions are shaped by nonspecifically adsorbed cations. We scrutinize the oxygen evolution reaction (OER) at nickel (oxy)hydroxide catalysts, using a physicochemical model that integrates density functional theory calculations, a microkinetic submodel, and a mean-field submodel of the electric double layer. The aptness of the model is verified by comparison with experiments. The robustness of model-based insights against uncertainties and variations in model parameters is examined, with a sensitivity analysis using Monto Carlo simulations. We interpret the decrease in OER activity with the increasing effective size of electrolyte cations as a consequence of cation overcrowding near the negatively charged electrode surface. The same reasoning could explain why the OER activity increases with solution pH on the RHE scale and why the OER activity decreases in the presence of bivalent cations. Overall, this work stresses the importance of correctly accounting for local reaction conditions in electrocatalytic reactions to obtain an accurate picture of factors that determine the electrode activity.

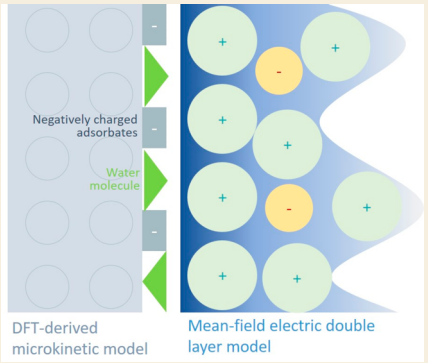

KEYWORDS: *Hydrogen production, Oxygen evolution reaction, Electrolyte cation effects, Local reaction condition, Surface charging effects, Electric double layer*

INTRODUCTION

Electrocatalysis is concerned, in the broadest sense, with the transformation between energy stored in chemical bonds and electrical energy. A hallmark of electrocatalysis is that the reaction rate, i.e., the rate of the transformation between chemical energy and electricity, can vary up to 10 orders of magnitude on different electrode materials.[1,2] The electrode dependence of the reaction rate is ascribed mainly to electronic interactions between the electrode and reaction intermediates.[1−3] A quintessential descriptor of electronic interactions is the binding energy of reaction intermediates.[1,4] It is an important and vibrant direction of research that the reaction rate can be enhanced by tuning this descriptor, e.g., via harnessing strain and ligand effects.[5,6]

Electrocatalytic reactions occur in a nanoscale interfacial region between the solid electrode and the electrolyte solution, termed electric double layer (EDL). Therefore, the reaction rate can also be tuned by modifying the composition of the electrolyte solution; relevant effects are termed electrolyte effects. Electrolyte effects have been observed in many electrocatalytic reactions, including hydrogen oxidation/evolution,[7−10] oxygen evolution/reduction,[7,11−14] methanol electro-oxidation,[15] and carbon dioxide reduction.[16,17] This work is concerned with the effects of electrolyte cations on the oxygen evolution reaction (OER), which is the performance-limiting anode reaction in electrochemical water splitting devices for hydrogen production.

The study of cation effects in the OER has a long history. Early studies were conducted by Erdey-Gruz and Shafarik in 1961 at platinum in 1 M H_2SO_4 with 0.3−1 M K^+, Na^+, Li^+, Zn^{2+}, Mg^{2+}, Al^{3+}, and NH_4^+[18] and by Kozawa in 1964 at several metals in 1 M NaOH with 0.1−10 mM Ba^{2+}, Cr^{2+}, and Ca^{2+}.[19] Erdey-Gruz and Shafarik observed that the activity decreases in the order $K^+ < Al^{3+} < NH_4^+ < Zn^{2+} < Na^+ < Mg^{2+} < Li^+$.[18] Kozawa found that the overpotential increases by 15−90 mV in the presence of 0.1−10 mM Ba^{2+}, Cr^{2+}, and Ca^{2+}.[19] Subsequent interest in the cation effects on the OER came from the field of alkaline batteries in the 1990s.[20−23] More recent interests are sparked by the study of cation effects on hydrogen oxidation reaction and oxygen reduction reaction by Strmcnik et al.[7]

Cation effects on OER at NiOOH thin films in both purified and Fe-containing alkaline electrolytes are of primary current interest, as Fe-doped NiOOH-based materials are promising catalysts for the OER. In 2015, Michael et al. observed the activity trend of $Cs^+ > K^+ > Na^+ \approx Li^+$ in purified electrolyte solutions and $K^+ \approx Na^+ > Cs^+ > Li^+$ in Fe-containing electrolyte solutions.[24] In 2017, Zaffran et al. observed that

Received: July 16, 2021
Published: September 30, 2021

alkaline earth cations (Mg^{2+} and Ca^{2+}) dramatically decrease the OER activity of NiOOH thin films in both purified and Fe-containing alkaline electrolyte solutions, a modern echo of the results of Kozawa reported more than 50 years ago.[25] Yang et al. further added tetraalkylammonium (TAA) cations into the comparison. They found an activity trend of $K^+ \approx Na^+ \approx TBA^+ > TMA^+ > Li^+$ for the OER at NiOOH thin films in purified alkaline electrolyte solutions and a different activity trend of $K^+ \approx Na^+ > TBA^+ > Li^+ > TMA^+$ in the presence of Fe impurities.[26] In 2019, Garcia et al. studied the effects of alkali metal cations on the OER at NiOOH thin films in both purified and Fe-containing alkaline electrolyte solutions. Their results show that the OER activity increases in the order of $Cs^+ > Na^+ > K^+ > Li^+$ in purified 0.1 M MOH (M = Cs, K, Na, Li), and $Cs^+ > K^+ > Na^+ > Li^+$ in the presence of Fe impurities.[14] Perini and Ticianelli reported an activity order of $K^+ > Na^+ > Li^+$ for the OER at gold.[27] The same order of activity is found for the OER at a $RuO_2(110)$ single-crystal by Rao et al.[28]

It is certainly fair to say that the understanding of cation effects in the OER is still incomplete. Most studies have been focusing on the interaction of electrolyte cations with the OER intermediates. In 2015, Michael et al. measured Raman spectra during the linear scanning voltammetry in purified LiOH and CsOH. However, they pointed out that the "precise mechanism by which CsOH promoted better catalytic performance than LiOH is unclear with results from this study."[24] In 2017, Zaffran et al. assumed that the electrolyte cations are intercalated into the layered NiOOH structure. Their computational results showed that intercalated Mg^{2+} and Ca^{2+} bind strongly to water and OER intermediates, thus decreasing the OER activity.[25] Yang et al. interpreted the cation effects from the perspective of interactions between cations and intermediates of the OER. They attributed the inhibition effect of TMA^+ on the OER activity to the specific interaction of TMA^+ with active oxygen-containing intermediates formed upon deprotonation.[26] Later, Garcia et al. identified $NiOO^-$ as the active oxygen-containing intermediate using in situ surface enhanced Raman spectroscopy (SERS). Further, they showed that $NiOO^-$ is better stabilized by larger cations Cs^+, which is believed to promote the OER.[14] Contrarily, Rao et al. attributed the higher OER activity in the case of K^+ to the weaker stabilization of active oxygen-containing intermediates, compared with Na^+ and Li^+, also using in situ SERS.[28] In addition, they found that the density of isolated water molecules not hydrogen-bonded to other water molecules is highest and the density of ice-like water molecules with four hydrogen bonds is lowest in the case of K^+, compared with the cases of Na^+ and Li^+. More isolated water molecules promote the OER activity, they conjectured.

In this work, we are concerned with the effect of nonspecifically adsorbed cations, such as alkali metal cations,[28] on the OER. The restriction to nonspecifically adsorbed cations allows us to focus on how electrolyte cations shape the local reaction conditions in the EDL that differ dramatically from bulk conditions. The local reaction conditions are deciphered using a model that integrates density-functional theory (DFT) calculations for elementary reaction steps, microkinetic modeling for multistep kinetics, and continuum modeling for the EDL structure. The model enables us to quantitatively correlate the OER activity and the effective cation size that considers the solvation shell. In addition, the model is extended to understand the effects of solution pH and bivalent alkaline earth cations on the OER activity. Given inevitable uncertainties and variations in model parameters, we conduct a sensitivity analysis study using Monte Carlo simulations to gauge the robustness of the model-based findings. This work adds to the understanding of how electrocatalytic activity of the electrode is influenced by the local reaction conditions.

METHODS

We adopt the concerted theory-computation framework, previously developed for oxygen reduction reaction by some of us,[29] for the present case of the OER. The framework is composed of three parts. In the first part, we determine the reaction mechanism using quantum-mechanical DFT calculations. In the second part, we treat the multistep kinetics using microkinetic modeling. In the third part, we use a continuum EDL model to calculate the local reaction conditions. These parts are interrelated. The microkinetic model, on the one hand, is based on the reaction mechanism determined from DFT calculations and, on the other hand, requires knowledge of the local reaction conditions that are determined from the EDL model. In turn, the EDL is influenced by interfacial reactions in that the surface charge density is a function of the coverages of reaction intermediates, which are the output of the microkinetic model. A consistent treatment of these models is a necessity for deciphering how electrolyte cations influence the OER and is also a unique feature of this work in comparison with similar models for the OER[30−32] and other electrocatalytic reactions.[33−35]

DFT Calculations

Spin-polarized periodic first-principles calculations based on density functional theory (DFT) were performed with the projector-augmented-wave (PAW)[36,37] method using the Vienna ab initio simulation package (VASP).[38−40] The Perdew−Burke−Ernzerhof (PBE) functional within the generalized gradient approximation (GGA) was used for exchange-correlation effects.[41] The wave functions were expanded by a plane wave basis with a kinetic cutoff energy of 750 eV. The DFT+U approach[42,43] was applied to correctly take account of the Coulomb interactions caused by the highly localized Ni 3d states of NiOOH, and the U-J value was set to be 5.5 eV, which was calculated by Li and Selloni.[44,45] Dispersion effects were taken into consideration using the DFT-D3 method.[46]

For the bulk optimization of NiOOH, a k-point mesh of $9 \times 9 \times 9$ was used to the integral over the first Brillouin zone. All atoms were relaxed upon optimization until the forces onto each atom were below 0.001 eV/Å. Here we used the bulk β-NiOOH structure from our previous work,[44] and the lattice parameters were calculated to be a = 2.92 Å, b = 5.84 Å, c = 4.82 Å (α = 69.40°, β = 109.75°, γ = 118.73°).

The β-NiOOH slab was modeled by the low-index (0001) termination in a three-layer slab with the bottom layer fixed and was represented by a (2×4) supercell. The uppermost two layers were fully relaxed until convergence was reached. The convergence criterion was set to be 0.01 eV/Å for the maximal force onto each relaxed atoms. The magnetic moment for each Ni atom was initialized to be 1 μB, and the resulting magnetic moments and related discussion are provided in section S4 of the Supporting Information (SI). A k-point mesh of $2 \times 2 \times 1$ was applied in the slab calculations. Dipole corrections were considered to compensate for the interaction between surface dipoles and their periodic images. A vacuum layer of 25 Å was used to avoid any spurious interactions normal to the surface.

To describe the energetics of the OER on the β-NiOOH surface, the grand canonical ab initio thermodynamics scheme[47,48] was used to evaluate the formation enthalpy of intermediates in solution. The computational hydrogen electrode (CHE) concept[49,50] was applied to calculate the electrochemical potential of H^+ in solution, μ_{H^+}, at a given electrode potential,

$$\mu_{H^+} + \mu_e = \frac{1}{2}\mu^0_{H_2} - eU_{SHE} - k_B T \ln(10)\mathrm{pH} = \frac{1}{2}\mu^0_{H_2} - eU_{RHE} \quad (1)$$

https://doi.org/10.1021/jacsau.1c00315
JACS Au 2021, 1, 1752−1765

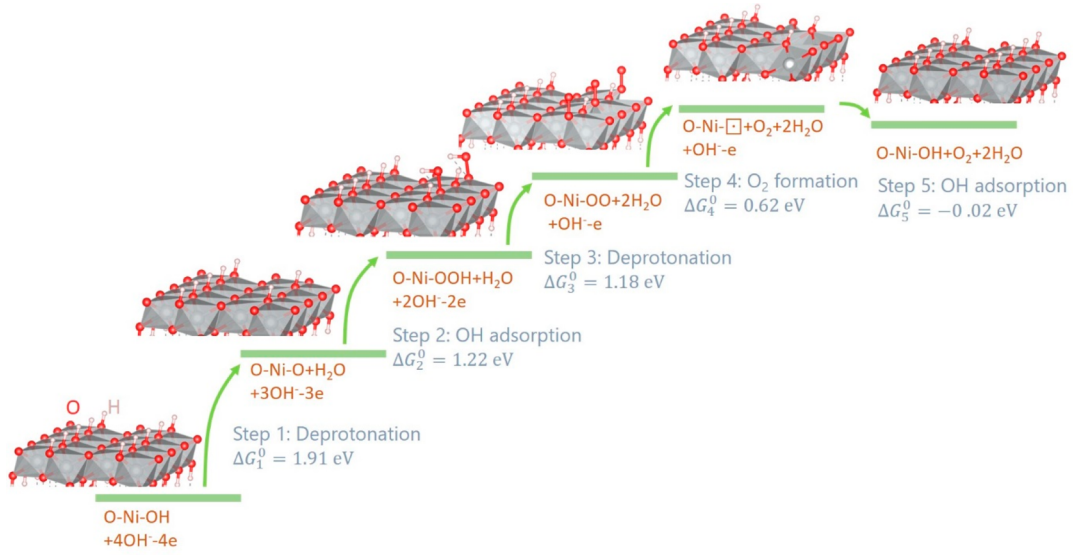

Figure 1. Gibbs free energy profile of OER on β-NiOOH (0001) surface calculated under standard conditions (298 K, pH = 0, 1 bar, 0 V_{SHE}).

where μ_e is the electrochemical potential of the electrons and $\mu^0_{H_2}$ that of hydrogen gas under standard conditions. U_{RHE} is the electrode potential on the reversible hydrogen electrode (RHE) scale. Using U_{RHE} instead of U_{SHE} versus the standard hydrogen electrode (SHE) aligns our results with the convention used in most experimental studies. The electrochemical potential of OH^- can be derived from

$$\mu_{OH^-} = \mu_{H_2O} - \mu_{H^+} \tag{2}$$

First, we calculated the Gibbs free energy change for each elementary step of the OER and explored the most favorable pathway under standard conditions (T = 298 K, pH = 0, p_{H_2} = 1 bar, 0 V_{SHE}). Multiple experimental studies have revealed that the original surface undergoes surface deprotonation prior to the OER.[14,51,52] Accordingly, the first step of the OER is thus

$$O{-}Ni{-}OH + OH^- \leftrightarrow O{-}Ni{-}O + H_2O + e \tag{3}$$

where O−Ni−OH represents the original surface and O−Ni−O is the (2 × 2) surface with 1/4 hydrogen atoms deprotonated.

The second step is the adsorption of a hydroxyl anion (OH^-) onto the deprotonated site, forming O−Ni−OOH,

$$O{-}Ni{-}O + OH^- \leftrightarrow O{-}Ni{-}OOH + e \tag{4}$$

Afterward, another OH^- approaches and removes one H from O−Ni−OOH,

$$O{-}Ni{-}OOH + OH^- \leftrightarrow O{-}Ni{-}OO + H_2O + e \tag{5}$$

followed by a chemical step releasing O_2, leaving the surface O−Ni−⊡ with an oxygen vacancy,

$$O{-}Ni{-}OO \leftrightarrow O - Ni{-}\boxdot + O_2 \tag{6}$$

Finally, the initial surface is recovered by filling the oxygen vacancy site with a OH^- in solution, completing the reaction cycle,

$$O{-}Ni{-}\boxdot + OH^- \leftrightarrow O{-}Ni{-}OH + e \tag{7}$$

The Gibbs free energy changes of the elementary steps as a function of the electrochemical control parameters were derived using the CHE method.[49,50] Steps 3, 4, 5, and 7 proceed via OH^- coupled electron transfer steps, for which we need the electrochemical potential of the electron−OH^- pair,

$$\mu_{OH^-} - \mu_e = \mu^0_{H_2O} - \frac{1}{2}\mu^0_{H_2} + eU_{RHE} \tag{8}$$

where μ_{OH^-} is the electrochemical potential of hydroxyl anions and $\mu^0_{H_2O}$ is that of liquid water under standard conditions. In order to compute $\mu^0_{H_2O}$ and $\mu^0_{H_2}$, we calculated the total energy of a single water molecule and a single hydrogen molecule using DFT and corrected for entropic contributions using entropy data from the NIST Chemistry Webbook.[53]

Consider, for example, the first deprotonation step. The Gibbs free energy change of this step at any potential U_{RHE} is calculated as

$$\begin{aligned}\Delta G_1 &= E_{O-Ni-O} + \mu^0_{H_2O} - E_{O-Ni-OH} - (\mu_{OH^-} - \mu_e) \\ &= (E_{O-Ni-O} - E_{O-Ni-OH}) + \frac{1}{2}\mu^0_{H_2} - eU_{RHE}\end{aligned} \tag{9}$$

where we used eq 8 for $(\mu_{OH^-}-\mu_e)$ and E_{O-Ni-O} and $E_{O-Ni-OH}$ represent the total energies of the O−Ni−O and O−Ni−OH surfaces calculated using quantum-mechanical DFT. The Gibbs free energy change of other steps can be calculated in the same manner, expressed as

$$\Delta G_2 = E_{O-Ni-OOH} - E_{O-Ni-OH} - \mu^0_{H_2O} + \frac{1}{2}\mu^0_{H_2} - eU_{RHE} \tag{10}$$

$$\Delta G_3 = E_{O-Ni-OO} - E_{O-Ni-OOH} + \frac{1}{2}\mu^0_{H_2} - eU_{RHE} \tag{11}$$

$$\Delta G_4 = E_{O-Ni-\boxdot} - E_{O-Ni-OO} + 4.92 + 2(\mu^0_{H_2O} - \mu^0_{H_2}) \tag{12}$$

$$\Delta G_5 = E_{O-Ni-OH} - E_{O-Ni-\boxdot} - \mu^0_{H_2O} + \frac{1}{2}\mu^0_{H_2} - eU_{RHE} \tag{13}$$

where we used $\mu^0_{O_2}$ = 4.92 eV+ $2(\mu^0_{H_2O}-\mu^0_{H_2})$, in eq 12.

The Gibbs free energy profile of the OER calculated under standard conditions (298 K, pH = 0, 1 bar, 0 V_{SHE}) is shown in Figure 1. The first deprotonation step has the most positive Gibbs free energy change, ΔG^0_1 = 1.91 eV, which means that it corresponds to the potential determining step, which is consistent with the results of Govind-Rajan et al.[54] The following four steps are energetically feasible at the equilibrium potential of the OER, E = 1.23 V_{RHE}. Especially, the NiO state with an oxygen vacancy is highly unstable and inclined to adsorb a OH^- from solution. Therefore, we combine the step 4 and 5 into a single step in the microkinetic model.

Microkinetic Model

A widely assumed reaction pathway of the OER in alkaline media proceeds via four OH^--coupled electron transfer steps,[55−57]

$$OH + OH^- \leftrightarrow O + H_2O + e \tag{14}$$

https://doi.org/10.1021/jacsau.1c00315
JACS Au 2021, 1, 1752−1765

$$O + OH^- \leftrightarrow OOH + e \tag{15}$$

$$OOH + OH^- \leftrightarrow OO + H_2O + e \tag{16}$$

$$OO + OH^- \leftrightarrow OH + O_2 + e \tag{17}$$

The reaction mechanism expressed in eqs 3−7 can be considered a specific case of the general mechanism, with eq 14 corresponding to eq 3, eq 15 to eq 4, eq 16 to eq 5, and eq 17 to the combination of eqs 6 and 7 because the NiO state is highly energetically unstable.

For the sake of generality, the microkinetic model is formulated for the mechanism expressed in eqs 14−17. The reaction rates are given by

$$v_1 = k_1^+[OH^-]'\theta_{OH} - k_1^-\theta_O \tag{18}$$

$$v_2 = k_2^+[OH^-]'\theta_O - k_2^-\theta_{OOH} \tag{19}$$

$$v_3 = k_3^+[OH^-]'\theta_{OOH} - k_3^-\theta_{OO} \tag{20}$$

$$v_4 = k_4^+[OH^-]'\theta_{OO} - k_4^-\theta_{OH} \tag{21}$$

Here, $[OH^-]'$ represents the concentration of OH^- at the reaction plane, which is to be determined from the EDL model; $k_i^\pm$ represent the forward (+) and backward (−) rate constants of the ith step, which are dependent on the local reaction condition provided by the EDL model; θ_{OH}, θ_O, θ_{OOH}, and θ_{OO} represent the coverages of reaction intermediates constrained by the conservation of surface sites,

$$\theta_{OH} + \theta_O + \theta_{OOH} + \theta_{OO} = 1 \tag{22}$$

According to transition state theory, the rate constants are given by

$$k_i^\pm = \frac{k_B T}{h}\exp\left(-\frac{G_{a,i}^\pm}{k_B T}\right) \tag{23}$$

where the activation barriers are related to the Gibbs free energies of reactions according to the Bronsted−Evans−Polanyi (BEP) relation,

$$G_{a,i}^+ = G_{a,i}^\ominus + \beta_i \Delta\Delta G_i, \quad G_{a,i}^- = G_{a,i}^\ominus - (1-\beta_i)\Delta\Delta G_i \tag{24}$$

where $G_{a,i}^\ominus$ is the activation barrier under standard equilibrium conditions (298 K, pH = 0, 1 bar), denoted by a superscript "⊖". $\Delta\Delta G_i$ represents the variation in the Gibbs free energies of reactions when the reaction condition deviates from the standard equilibrium conditions. We shall also specify the coverages of adsorbates under the standard equilibrium conditions, if we attempt to consider the coverage-dependence of $\Delta\Delta G_i$. In our DFT calculations, we have $\theta_O^\ominus = \theta_{OO}^\ominus = \theta_{OOH}^\ominus = 1/4$ because one of the four sites in the supercell is subject to surface reactions, and $\theta_{OH}^\ominus = 1$ for the original surface.

Under any reaction condition, $\Delta\Delta G_i$ is given by

$$\Delta\Delta G_1 = -e_0(\phi_M - \phi' - U_1^\ominus) + \Delta\Delta G_O - \Delta\Delta G_{OH} \tag{25}$$

$$\Delta\Delta G_2 = -e_0(\phi_M - \phi' - U_2^\ominus) + \Delta\Delta G_{OOH} - \Delta\Delta G_O \tag{26}$$

$$\Delta\Delta G_3 = -e_0(\phi_M - \phi' - U_3^\ominus) + \Delta\Delta G_{OO} - \Delta\Delta G_{OOH} \tag{27}$$

$$\Delta\Delta G_4 = -e_0(\phi_M - \phi' - U_4^\ominus) + \Delta\Delta G_{OH} - \Delta\Delta G_{OO} \tag{28}$$

where ϕ_M represents the electrode potential on the SHE scale and ϕ' is the potential at the reaction plane in solution relative to the electric potential in the solution bulk which is taken as the potential reference.

$U_i^\ominus$'s, the standard equilibrium potentials of the reaction steps in eqs 14−17 versus the RHE, are given by

$$U_1^\ominus = \frac{1}{e_0}\left(E_{O-Ni-O} - E_{O-Ni-OH} + \frac{1}{2}\mu_{H_2}^0\right) \tag{29}$$

$$U_2^\ominus = \frac{1}{e_0}\left(E_{O-Ni-OOH} - E_{O-Ni-OH} - \mu_{H_2O}^0 + \frac{1}{2}\mu_{H_2}^0\right) \tag{30}$$

$$U_3^\ominus = \frac{1}{e_0}\left(E_{O-Ni-OO} - E_{O-Ni-OOH} + \frac{1}{2}\mu_{H_2}^0\right) \tag{31}$$

$$U_4^\ominus = \frac{1}{e_0}\left(E_{O-Ni-OH} - E_{O-Ni-OO} + 4.92\ \text{eV} + \mu_{H_2O}^0 - \frac{1}{2}\mu_{H_2}^0\right) \tag{32}$$

based on eqs 9−13.

$\Delta\Delta G_i$ in eqs 25−28 accounts for the variation in Gibbs free energies of the reaction intermediates OH, O, OOH, and OO when ϕ_M changes. There are multiple reasons for such variations. On the one hand, θ_{OH}, θ_O, θ_{OOH}, and θ_{OO} change with ϕ_M, so the Gibbs free energy of adding a new intermediate changes due to lateral interactions of the new intermediate with existing ones.[58] On the other hand, the local electric potential and electric field change with ϕ_M, altering the Gibbs free energy of intermediates that carry a net charge. The Frumkin adsorption isotherm uses an empirical coefficient, called the lateral interaction coefficient, to describe the linear relation between $\Delta\Delta G_X$ and θ_X. The linear relation is a first approximation. In addition, the Frumkin adsorption isotherm usually neglects interactions among adsorbed intermediates of different kinds. Norskov and co-workers expressed $\Delta\Delta G_X$ as a function of the electric field, whose coefficients are fitted from DFT calculations.[59,60] In an empirical sense, the Frumkin adsorption isotherm and the relation of Norskov and co-workers are equivalent, as there exists a one to one correspondence between θ_X and the electric field, both of which are uniquely determined by ϕ_M. Herein, we use

$$\Delta\Delta G_X = \mu_X E_{AP} \tag{33}$$

with μ_X being an empirical dipole moment of intermediate X and E_{AP} being the electric field strength at the adsorbate plane (AP). As will be made clear in the EDL model, E_{AP} is co-determined by all existing adsorbed intermediates. Therefore, eq 33 effectively considers interactions among adsorbed intermediates of all kinds.

At steady state, we have

$$v_1 = v_2 = v_3 = v_4 = \frac{j_{OER}}{4e_0\rho_s} \tag{34}$$

where j_{OER} is the current density of the OER and ρ_s the number density of active sites.

We can solve for the coverages,

$$\theta_{OH} = \frac{1}{\Xi}\left(\frac{1}{k_4^-} + \frac{K_4}{k_3^-} + \frac{K_3K_4}{k_2^-} + \frac{K_2K_3K_4}{k_1^-}\right)$$

$$\theta_O = \frac{1}{\Xi}\left(\frac{1}{k_1^-} + \frac{K_1}{k_4^-} + \frac{K_1K_4}{k_3^-} + \frac{K_1K_4K_3}{k_2^-}\right)$$

$$\theta_{OOH} = \frac{1}{\Xi}\left(\frac{1}{k_2^-} + \frac{K_2}{k_1^-} + \frac{K_2K_1}{k_4^-} + \frac{K_2K_1K_4}{k_3^-}\right)$$

$$\theta_{OO} = \frac{1}{\Xi}\left(\frac{1}{k_3^-} + \frac{K_3}{k_2^-} + \frac{K_3K_2}{k_1^-} + \frac{K_3K_2K_1}{k_4^-}\right) \tag{35}$$

with $K_i = k_i^{+*}/k_i^-$, $k_i^{+*} = k_i^+[OH^-]'$, and Ξ,

$$\Xi = \frac{1 + K_1 + K_1K_2 + K_1K_2K_3}{k_4^-} + \frac{1 + K_4 + K_4K_1 + K_4K_1K_2}{k_3^-} + \frac{1 + K_3 + K_3K_4 + K_3K_4K_1}{k_2^-} + \frac{1 + K_2 + K_2K_3 + K_2K_3K_4}{k_1^-} \tag{36}$$

The current density is transformed to,

$$\frac{4e\rho_s}{j_{OER}} = \frac{\Theta_1}{k_1^{+*}} + \frac{\Theta_2}{k_2^{+*}} + \frac{\Theta_3}{k_3^{+*}} + \frac{\Theta_4}{k_4^{+*}} \tag{37}$$

with the thermodynamic factors

https://doi.org/10.1021/jacsau.1c00315
JACS Au 2021, 1, 1752−1765

$$\Theta_1 = \frac{1 + K_2 + K_2K_3 + K_2K_3K_4}{K_2K_3K_4}$$
$$\Theta_2 = \frac{1 + K_3 + K_3K_4 + K_3K_4K_1}{K_1K_3K_4}$$
$$\Theta_3 = \frac{1 + K_4 + K_4K_1 + K_4K_1K_2}{K_1K_2K_4}$$
$$\Theta_4 = \frac{1 + K_1 + K_1K_2 + K_1K_2K_3}{K_1K_2K_3} \quad (38)$$

Electric Double Layer Model

We require an EDL model to compute the local reaction conditions, including ϕ', $[OH^-]'$, and E_{AP}. The mean-field Helmholtz free energy per unit volume of the electrolyte solution is written as[61,62]

$$f_{es} = e_0\phi(N_c - N_a) - \frac{\epsilon_\infty E^2}{2} - \frac{1}{\beta}N_s \ln\left(\frac{\sinh(pE\beta)}{pE\beta}\right) + \frac{1}{\beta}\ln\frac{N!}{N_c!N_a!N_s!} \quad (39)$$

where e_0 is the elementary charge, ϵ_∞ is the optical component of the dielectric constant, ϕ is the potential, $E = \nabla\phi$ is the electrical field, $\beta = 1/k_BT$ is the inverse thermal energy, p is the dipole moment of solvent molecules, N is the total number density of lattice sites, and N_i (i = s, a, c) are the number densities of solvent molecules (s), anions (a), and cations (c). On the right-hand side of eq 39, the first term is the electrostatic free energy of ions, the second term is the self-energy of the electric field, the third term is the electrostatic free energy of solvent molecules, and the last term is the entropic free energy related to the configuration of solution species, which is calculated using a lattice-gas approach. The conservation of lattice sites leads to $N_s = N - N_a - N_c$.

Based on the variational principle, we obtain the following Euler–Lagrange equation in terms of ϕ,

$$\frac{\partial f_{es}}{\partial\phi} - \frac{\partial}{\partial x}\left(\frac{\partial f_{es}}{\partial E}\right) = 0 \quad (40)$$

leading to a modified Poisson–Boltzmann (PB) equation,

$$-\frac{\partial}{\partial x}\left(\epsilon_\infty + \frac{pN_s}{E}L\left(\frac{pE}{k_BT}\right)\right)E = e_0(N_c - N_a) \quad (41)$$

where $L(x) = \coth(x) - 1/x$ is the Langevin function. Compared with the conventional PB equation, eq 41 features an electric field-dependent local dielectric constant. Equation 41 has been derived in the dipolar Poisson–Boltzmann model by Abrashkin et al.[63] and the Langevin–Poisson–Boltzmann model by Gongadze and Iglic.[64]

The distributions of cations and anions are obtained from

$$\frac{\partial f_{es}}{\partial N_c} = \left(\frac{\partial f_{es}}{\partial N_c}\right)_{bulk} \quad (42)$$

$$\frac{\partial f_{es}}{\partial N_a} = \left(\frac{\partial f_{es}}{\partial N_a}\right)_{bulk} \quad (43)$$

Equations 42 and 43 say that electrochemical potentials of cations and anions in the EDL are uniform and thus equal to their bulk values. Substituting eq 39 into eqs 42 and 43 leads toone of

$$N_c = \frac{N\chi\exp(-\beta e_0\phi)}{\chi\gamma_c\exp(-\beta e_0\phi) + \chi\gamma_a\exp(\beta e_0\phi) + (1-2\chi)\frac{\sinh(pE\beta)}{pE\beta}} \quad (44)$$

$$N_a = \frac{N\chi\exp(\beta e_0\phi)}{\chi\gamma_c\exp(-\beta e_0\phi) + \chi\gamma_a\exp(\beta e_0\phi) + (1-2\chi)\frac{\sinh(pE\beta)}{pE\beta}} \quad (45)$$

where χ is the bulk number density of cations/anions normalized to N, and γ_a and γ_c denote relative sizes of solvated anions and cations, respectively, calculated as

$$\gamma_{a,c} = \left(\frac{d_{a,c}}{d_s}\right)^3 \quad (46)$$

with $d_{a,c}$ being the effective diameters of solvated anions and cations and d_s being the diameter of solvent molecules, which is taken as the reference size of the lattice. We stress that eqs 44 and 45 take into account the ion size effect in a phenomenological manner, namely, by introducing two size factors γ_a and γ_c. A more rigorous treatment of the size effect can be found in ref 65.

Substituting eqs 44 and 45 into eq 41 leads to a single differential equation governing the distribution of electric potential. Its boundary conditions are as follows:

$$\phi = 0 \quad (47)$$

in the solution bulk and

$$\phi = \phi_M - \phi_{pzc} + \delta_{AP}E_{AP} \quad (48)$$

at the adsorbate plane (AP), which is designated as the coordinate origin, $x = 0$, of the EDL model. The space between the electrode surface and the adsorbate layer has a thickness of δ_{AP}, a permittivity of ϵ_{AP}, and an electric field of E_{AP}. ϕ_{pzc} is the potential of zero charge. The third term on the right-hand side (RHS) of eq 48 represents the potential drop across the adsorbate layer, where the uniform electric field E_{AP} is given by[66,67]

$$E_{AP} = \frac{\epsilon}{\epsilon_{AP}}\frac{\partial\phi}{\partial x} + \frac{\mu_{chem}}{\epsilon_{AP}\delta_{AP}} \quad (49)$$

where the first term on the RHS represents the electric field caused by the excess free charge on the electrode surface and the second term represents the electric field generated by the dipole moment formed between charged intermediates and its compensating charge in the electrode, denoted by μ_{chem},[66,67]

$$\mu_{chem} = \sum_{X=OH,O,OOH,OO}\theta_X\xi_X\delta_{AP}\rho_s \quad (50)$$

where ξ_X is the net charge number of adsorbed intermediates.

Model Parameters and Numerical Implementation

Table 1 lists the model parameters which are categorized into five subgroups termed "general constants", "electrode", "electrolyte solution", "interfacial structure", and "reaction". The electrode parameters correspond to β-NiOOH (0001). The (2 × 2) supercell has a surface area of S_{sc} = (5.85 Å × 10.24 Å) = 59.90 Å^2, according to the DFT calculation. Therefore, the number density of reaction sites equals $\rho_s = \frac{4}{S_{sc}} = 6.67 \times 10^{18}\,m^{-2}$. The work function of the slab surface with one layer of water molecules is calculated to be Φ = 5.6 eV.[44] Therefore, the pzc versus the SHE is calculated as $\phi_{pzc} = \frac{\Phi}{e_0} - 4.44 = 1.16V_{SHE}$, assuming that the absolute electrode potential of the SHE is 4.44 eV.

The electrolyte parameters correspond to 0.1 M MOH (M = Li, Na, Cs). From the expression of the effective dielectric constant given in eq 41, we obtain the bulk dielectric constant as $\epsilon_b = \epsilon_\infty + \frac{1}{3}\frac{p^2N_s^b}{k_BT}$. Therefore, the effective dipole moment of water molecules is found as $\sqrt{\frac{3k_BT(\epsilon_b - \epsilon_\infty)}{c_s^bN_A}}$. The effective size of solvated ions can be controversial, due to the complicated solvation structure of ions and the uncertainty in defining the effective size. Herein, we cite Israelachvili's list of hydrated radii of ions in water, d_a = 3.0 Å for hydrated OH^- and d_c =

https://doi.org/10.1021/jacsau.1c00315
JACS Au 2021, 1, 1752–1765

Table 1. Model Parameters for the Base Case

general constants		
k_B, Boltzmann constant		1.38×10^{-23} J/K
e_0, elementary charge		1.6×10^{-19}C
N_A, Avogadro constant		6.02×10^{23}/mol
ϵ_0, vacuum permittivity		8.85×10^{-11} F/m
ϵ_b, permittivity of bulk water		$78.5\epsilon_0$
h, Planck constant		6.626×10^{-34} J/s
T, temperature		298.15 K
electrode		
ρ_s, the number density of reaction sites	$6.67 \times 10^{18}/m^2$	DFT calculation
Φ, work function of the solvated electrode	5.6 eV	DFT calculation[44]
ϕ_{pzc} vs RHE, potential of zero charge	$\frac{\Phi}{e_0} - 4.44 + \ln 10\frac{k_B T}{e_0}$pH	absolute electrode potential of the SHE is 4.44 eV
electrolyte solution		
d_s, diameter of water molecules	2.75 Å	
d_a, effective diameter of solvated anions	6.0 Å	
d_c, effective diameter of solvated cations	7.6, 7.2, 6.6, 6.6 Å for Li^+, Na^+, K^+, Cs^+	
ϵ_∞, optical permittivity	ϵ_0	
p, effective dipole moment of water molecules	$\sqrt{\frac{3k_B T(\epsilon_b - \epsilon_\infty)}{c_s^b N_A}}$	
c_s^b, bulk concentration of water	55.5 M	
pH	13	
$c_{a/c}^b$, bulk concentration of anions/cations	0.1 M	
N, total number density of lattice sites	$(c_s^b + c_a^b + c_c^b)N_A$	
χ, bulk number density of cations/anions normalized to N	$\frac{c_a^b N_A}{N}$	
interfacial structure		
ϵ_{AP}, permittivity of the adsorbate layer		$4\epsilon_0$
δ_{AP}, thickness of the adsorbate layer		1.5 Å
reaction		
$U_i^\ominus$, standard equilibrium potentials of the reaction steps versus RHE	1.92, 1.22, 1.18, 0.60 V for eqs 14−17, respectively	DFT calculation
β_i, transfer coefficient	0.5	
$G_{a,i}^\ominus$, activation barrier under the standard equilibrium conditions	0.50, 0.33, 0.31, 0.44 eV for eqs 14−17, respectively	fitted
μ_X, empirical dipole moment of intermediate X	$\xi_X e_0 \delta_{AP}$	fitted
ξ_X, net charge number of adsorbed intermediates	−0.06, −0.01, −0.04, −0.04 for OH, O, OOH, OO, respectively	fitted

7.6, 7.2, 6.6, and 6.6 Å for hydrated Li^+, Na^+, K^+, and Cs^+, respectively.[68] The adopted values are close to the Stokes radii of hydrated ions in water from ionic conductivity measurements.[10]

As a first approximation, we assume that all adsorbates line up rigidly in the adsorbate layer and are equidistant from the electrode surface. The thickness of the adsorbate layer is δ_{AP} = 1.5 Å as the mean value of the sizes of OH, O, OOH, and OO. The permittivity of the adsorbate layer is usually assumed to be a multiple of the vacuum permittivity, and here we inherit $\epsilon_{AP} = 3\epsilon_0$ from ref 67.

The standard equilibrium potentials of the reaction steps versus the RHE are calculated from eqs 29−32 with E_{O-Ni-O}, $E_{O-Ni-OOH}$, $E_{O-Ni-OO}$, $E_{O-Ni-\square}$, $\mu_{H_2O}^0$, and $\mu_{H_2}^0$ obtained from DFT calculations. The Kohn−Sham DFT approach implemented with PBE and RPBE exchange-correlation functionals has a typical root-mean-square deviation of ∼0.3 eV for chemisorbed systems.[69] The error shall grow in electrochemical systems with the presence of the electrolyte solution. In addition, we have neglected the zero-point energy corrections; see the discussion in section S3 in the SI. Therefore, the values of $U_i^\ominus$ calculated with DFT results are allowed to vary in the range of ∼0.3 V. The transfer coefficients of the reaction steps are taken as β_i = 0.5. Microscopically, β_i shall vary as a function of ϕ_M and vary from reaction to reaction.[70,71] In ref 70, Huang derived an analytical expression for β_i where different factors are discriminated. However, since we use the phenomenological Butler−Volmer equations for the elementary step kinetics, we should not be bothered by mechanistic complexities of β_i. The nudged elastic band (NEB) method can be used to calculate activation barriers of electrocatalytic reactions.[72] Herein, we choose to fit the activation barriers from experimental polarization data, considering that the error in DFT calculations at the transition state should be larger than that at the ground state, namely, >0.3 eV. The net charge numbers of adsorbed intermediates ξ_X are also fitted from experimental data. The fitting details are provided in section S1 of the SI. The sensitivity of the fitted parameters will be gauged at a latter point in the Discussion section. The numerical implementation of the model was performed in MATLAB. The code script is available upon request. We note that all potentials are rescaled to the RHE in the model calculation.

RESULTS

In this section, we describe how the local reaction conditions are shaped by the cations in the first subsection, which lays the basis for understanding the cation effects on the OER in the second subsection. Afterward, we discuss other means to tune the cation effects, including the solution pH in the third subsection and bivalent cations in the last subsection.

Local Reaction Conditions

The local reaction conditions computed by the model are shown in Figure 2, where the effective diameter of the cations d_c is varied between 4 and 8 Å with a step of 0.4 Å and 11 lines are included in each figure. Figure 2a−c exhibits the spatial distributions of OH^- concentration ($[OH^-]$), cation concentration($[C^+]$), and dielectric constant (ϵ) in the EDL at ϕ_M = 1.6 V_{RHE}, respectively. Let us first analyze general trends and then dissect differences among different lines corresponding to different d_c's.

$[OH^-]$ decreases from the bulk solution to the electrode surface because the surface charge density σ is negative even at this high electrode potentials (see Figure 2d) and OH^- ions are repelled as co-ions away from the electrode surface. σ is negative in the considered potential range because the pzc is 1.93 V_{RHE} for pH = 13, which is consistent with the fact that the point of zero charge of $Ni(OH)_2$ is ∼11 (namely, the solid will be negatively charged at pH > 11) .[73] Consequently, cations are attracted as counterions by the negative surface charge, resulting in an increasing profile of $[C^+]$ toward the electrode surface. In addition, ϵ decreases toward the electrode surface, which is ascribed to the combined effect of polarization saturation due to the high interfacial electric field and density decrement due to the crowding of counterions. The monotonically decreasing trend of ϵ in the EDL has been revealed by Nakayama and Andelman,[74] and Gongadze and Iglič.[64] In a previous work, Huang, Chen, and Eikerling showed nonmonotonic profiles of ϵ in the EDL due to the competition between ions and solvent molecules.[62] The nonmonotonic behavior is more pronounced in the presence of specific ion adsorption.

As d_c increases, fewer cations can accumulate in the EDL and $[C^+]$ decreases accordingly, as shown in Figure 2b. Moreover, the black line corresponding to d_c = 8 Å levels off

https://doi.org/10.1021/jacsau.1c00315
JACS Au 2021, 1, 1752−1765

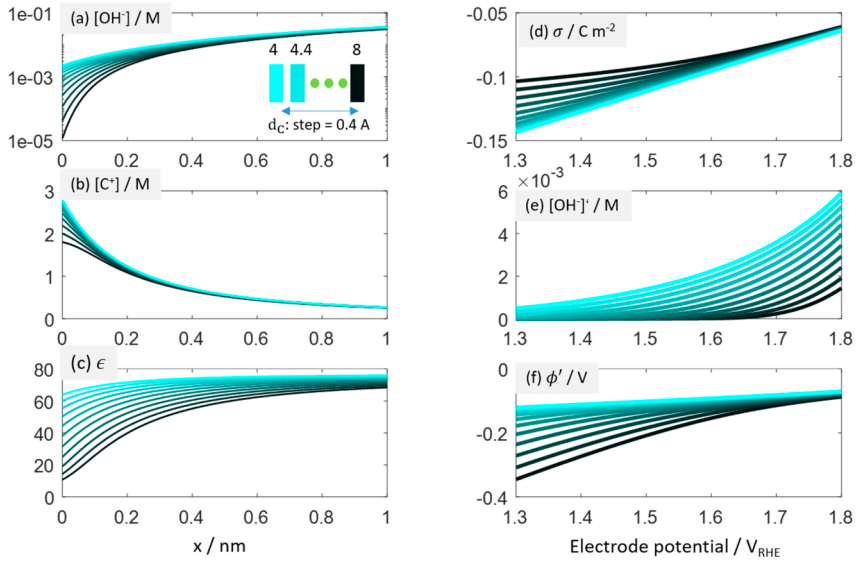

Figure 2. Local reaction conditions of the OER with the effective cation diameter d_c varying between 4 and 8 Å with a step of 0.4 Å. (a–c) Distribution of OH^- concentration ($[OH^-]$), cation concentration ($[C^+]$), and dielectric constant (ϵ) in the EDL at ϕ_M = 1.6 V_{RHE}, respectively. The coordinate origin x = 0 corresponds to the outer plane of the adlayer. (d–f) Variation of surface charge density (σ), OH^- concentration at x = 0 ($[OH^-]'$), and electric potential at x = 0 (ϕ') as a function of ϕ_M, respectively. Model parameters are listed in Table 1.

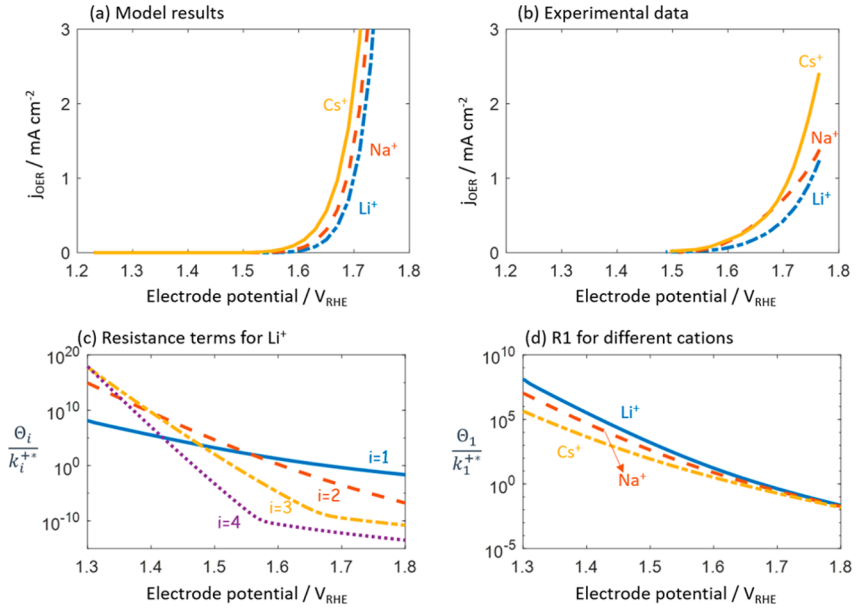

Figure 3. Model-experiment comparison. (a) Model-calculated polarization curves for OER in 0.1 MOH (M = Li^+, Na^+, Cs^+) with model parameters listed in Table 1. (b) Experimental polarization curves under the same condition measured by Michael et al.[24] (c) Four resistance terms $\frac{\Theta_i}{k_i^{+*}}$ in eq 37 as a function of the electrode potential for the case of M = Li^+. (d) Rate-determining resistance above 1.6 V_{RHE}, $\frac{\Theta_1}{k_1^{+*}}$, for different cations.

near the electrode surface, signifying the overcrowding phenomenon of cations.[75] Due to the intensified steric repulsion of cations, both $[OH^-]$ and ϵ decrease for larger d_c; see Figure 2a and c, respectively. From now on, the cation overcrowding effects are referred to as effects caused by the substantial accumulation of cations near the electrode surface due to the negative surface charge, including decreased $[OH^-]$, lower ϵ and among others.

Figure 2d–f exhibits the variation of surface charge density (σ), OH^- concentration at x = 0 ($[OH^-]'$), and electric potential at x = 0 (ϕ') as a function of ϕ_M, respectively. σ increases toward positive values and $[OH^-]'$ grows with increasing ϕ_M. The larger the cation size, the smaller the magnitude of σ. The dependence of σ on the cation size is readily understood from the effective thickness of the diffuse layer, which becomes thicker for larger cations, resulting in a smaller magnitude of σ. A similar analysis is provided by Ringe et al. for cation effects in carbon dioxide reduction.[76] For the case of a larger d_c, $[OH^-]'$ decreases due to greater steric repulsion because the size factor γ_c is cubic with d_c, despite the decreasing magnitude of σ. Figure 2e shows that the local electric potential ϕ' follows the positive-shift trend of σ with increasing ϕ_M and grows in magnitude with increasing d_c due to diminished screening effect of water molecules, Figure 2c.

https://doi.org/10.1021/jacsau.1c00315
JACS Au 2021, 1, 1752–1765

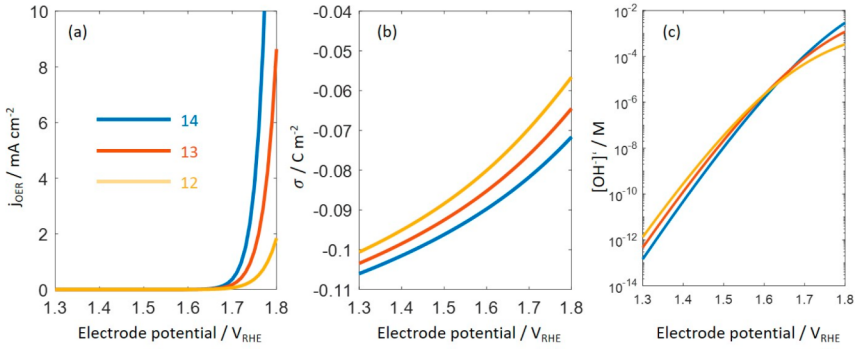

Figure 4. (a) pH effect of the OER in x (x = 1, 0.1, 0.01) M LiOH with the total ionic strength kept at 1 M. (b) Surface charging relation for the three pHs. (c) OH^- concentration at the reaction plane as a function of the electrode potential for the three pHs.

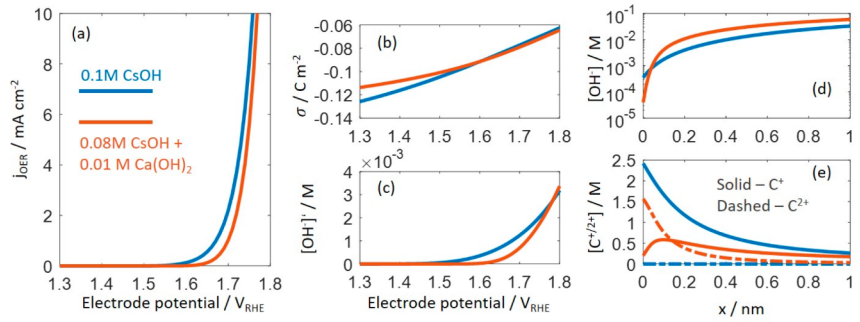

Figure 5. (a) Influence of bivalent cations (Ca^{2+}) on the OER. Two electrolyte solutions are compared, including 0.1 M CsOH (blue) of 0.08 M CsOH + 0.01 M $Ca(OH)_2$ (red). The OH^- concentration is kept at 0.1 M for both electrolyte solutions. (b) Comparison of the surface charging relation. (c) Comparison of the OH^- concentration at the reaction plane as a function of the electrode potential. (d) Spatial distribution of OH^- concentration at 1.6 V_{RHE}. (e) Spatial distribution of monovalent (solid lines) and bivalent cations (dashed lines) at 1.6 V_{RHE}.

Model-Experiment Comparison

With a knowledge of cation effects on the local reaction conditions, we proceed to analyze cation effects on the polarization curve, namely, the voltage−current relation. Figure 3a shows that the exponential growth in j_{OER} with increasing ϕ_M is deferred for Li^+ compared with Cs^+, which is consistent with experimental data, Figure 3b.[14,24] However, we also notice deviations in the details of the polarization curves between the model and experiments. Possible causes for the deviations are many, including the deviation between the idealized β-NiOOH(0001) slab and the actual surface states of the oxide, the deviation between the phenomenological Butler−Volmer equation and the complicated electron transfer kinetics, and the neglect of mass transport effects in this model. In Figure S2, we compare the polarization curves of OER at NiOOH in purified 0.1 MOH (M = Li^+, Na^+, Cs^+) measured by two laboratories.[14,24] Though the activity trend of Cs^+ > Na^+ > Li^+ is shared by both, noticeable deviations in the magnitude of the current density and the detailed profiles of the polarization curves are found. Nevertheless, the deviations in details of the polarization curves between the model and experiments in Figure 3 and between two experimental studies in Figure S2 shall not prevent us from understanding the trend of cation effects on the OER.

The microkinetic model enables us to gain deep insights into the reaction mechanism. Figure 3c shows the variation of different resistance terms $\frac{\Theta_i}{k_i^{+*}}$ (i = 1−4) in eq 37 as a function of ϕ_M. The rate-determining term (RDT) transitions from the third term i = 3 to the second term and then to the first term as ϕ_M increases. The RDT above 1.6 V_{SHE}, namely, the first term, grows in the order Cs^+ < Na^+ < Li^+ (Figure 3d), leading to the catalytic activity decreasing in the order Cs^+ > Na^+ > Li^+ (Figure 3a). The reason is simply that larger cations occupy more volume near the negatively charged surface, leading to a smaller concentration of OH^-, the reactant (Figure 2a). In Figure S1, we analyze an extreme case where the activation energy of the first step is increased to 0.98 eV, around 0.6 eV higher than other steps, to provide the readers an example of how this model behaves in extreme cases.

pH Effects

For proton-coupled electron transfer (PCET) reactions, under thermodynamic equilibrium conditions, the reaction should be invariant on the RHE scale.[77,78] Therefore, any observed pH effects on the RHE scale are usually ascribed to decoupled proton and electron transfer reactions.[79] Note that our current model goes beyond such a purely thermodynamic analysis. We will show below thatmicrokinetic considerations influenced by double-layer effects bring new insights into the pH effects in the OER.

Figure 4a shows that the OER activity on the RHE scale increases with increasing pH, consistent with experimental data.[79,80] The total ionic strength is 1 M for all pH values considered. The pH-dependent trend in activity contrasts with a thermodynamic analysis that predicts a pH-independent activity on the RHE scale as all elementary steps are PCET reactions in our model.[77] The discrepancy lies in the EDL effects. Figure 4b shows that σ is more negative at higher pHs, which can be effectively understood by the fact that the pzc on the RHE scale increases with pH. Therefore, the cation overcrowding effect is more pronounced at higher pHs,

https://doi.org/10.1021/jacsau.1c00315
JACS Au 2021, 1, 1752−1765

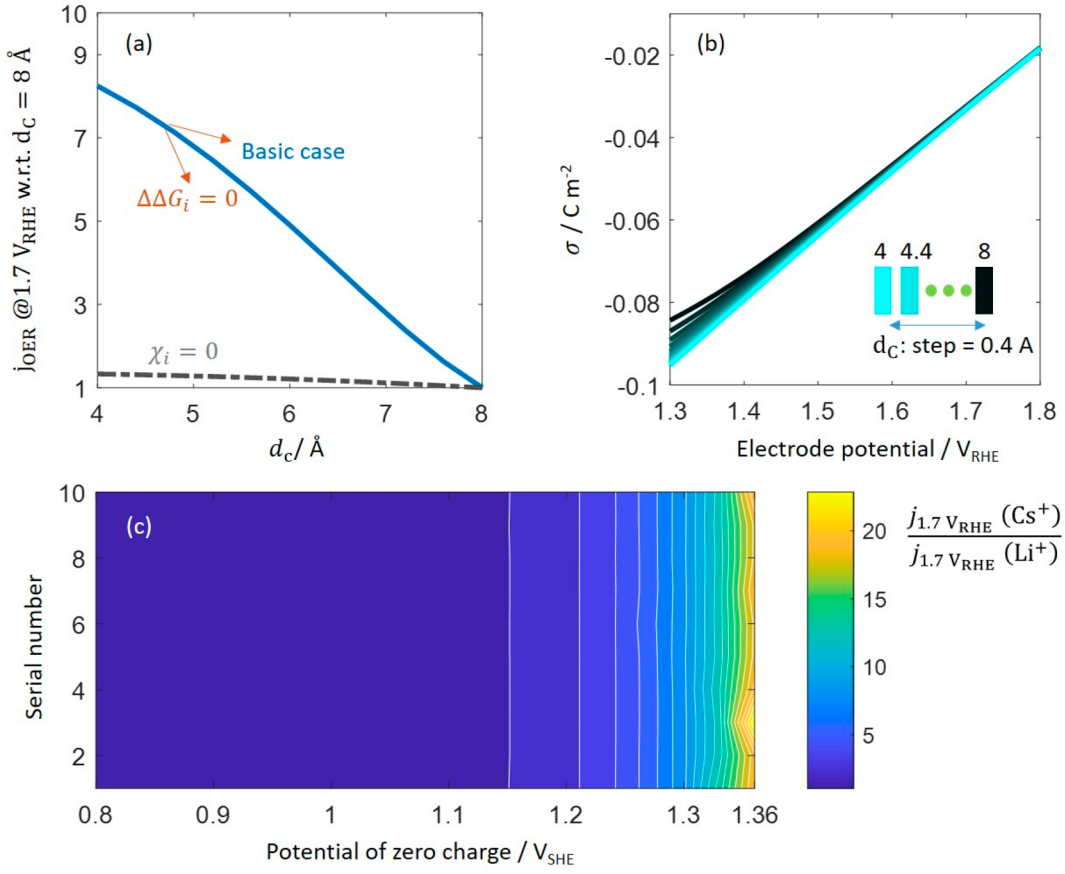

Figure 6. (a) Comparison between the base case, the case without dipole corrections for the binding energies ($\Delta\Delta G_i = 0$), and the case without chemisorption-induced surface dipoles ($\chi_i = 0$). The vertical axis represents the OER current density at 1.7 V_{RHE} for a particular value of d_c referenced to that for d_c = 8 Å. (b) Surface charging relation for the case without chemisorption-induced surface dipoles. (c) OER current ratio between Cs^+ and Li^+ at 1.7 V_{RHE}. The *x*-axis is the potential of zero charge. The *y*-axis is the serial number of simulations in which $U_1^{\ominus}$, $U_2^{\ominus}$, $U_3^{\ominus}$ are allowed to vary randomly within 0.2 V around their base values, with $U_4^{\ominus} = 4.92 - U_1^{\ominus} - U_2^{\ominus} - U_4^{\ominus}$.

resulting in a lower $[OH^-]'$ at potentials below 1.6 V_{RHE}, even though the bulk OH^- concentration is greater at higher pHs. σ is less negative with increasing ϕ_M, alleviating the cation overcrowding effect and leading to larger $[OH^-]'$ for higher pHs at potentials above 1.6 V_{RHE}. Since the OER activity is limited by $[OH^-]'$ that is dictated by the cation overcrowding effect, the OER activity thus grows with increasing pH at potentials above 1.6 V_{RHE}, see Figure 4a.

Bivalent Cation Effects

Adding bivalent cations into the solution while retaining the same OH^- concentration, we observe a decrement in the OER activity, as shown in Figure 5a, which is consistent with the experimental observations.[19,25] The underlying causes are related to the modifications to the EDL by the bivalent cations. Figure 5b exhibits the surface charging curves. Specifically, σ is slightly more negative above 1.6 V_{RHE} in the presence of Ca^{2+}. Due to the larger size of Ca^{2+} (8.2 Å in diameter), $[OH^-]'$ is lower in the presence of Ca^{2+}, Figure 5c, leading to the lower OER activity in Figure 5a. Figure 5d and e show the spatial distributions of OH^- concentration and cation concentrations in the EDL at 1.6 V_{RHE}. As bivalent cations are more effective in screening the electric field, the concentration of Ca^{2+} is greater near the electrode surface than that of Cs^+. Consequently, the OH^- concentration near the electrode surface is lower in the presence of Ca^{2+} (Figure 5d).

DISCUSSION

In this section, we first compare electronic and electrostatic factors regarding the cation effects. Then, we gauge the robustness of the model results in the vast parameter space by examining the sensitivity of the model output to the variation/uncertainty of the model parameters. Finally, we dissect the features and limitations of the model and discuss the extensions needed when applied to other catalysts and reactions.

Electronic vs Electrostatic Factors

The model considers both electronic and electrostatic factors. The former type is reflected in the binding energies under standard conditions and dipole corrections, namely, the $\Delta\Delta G_i$ terms. The latter type includes local electric potential and concentrations that are influenced by electrostatic interactions. The critical property governing the electrostatic interactions is the surface charge density, which is modified by chemisorption-induced surface dipoles (μ_{chem}). In this section, we compare the importance of electronic and electrostatic factors for cation effects in the OER.

In Figure 6a, we compare three cases, including the base case, the second case without dipole corrections for the binding energies ($\Delta\Delta G_i = 0$), and the third case without chemisorption-induced surface dipoles that is realized by setting $\chi_i = 0$. The comparison is made in terms of the OER current density at 1.7 V_{SHE} for a series of d_c referenced to that

https://doi.org/10.1021/jacsau.1c00315
JACS Au 2021, 1, 1752−1765

for d_c = 8 Å. All curves show that the OER current density decreases as d_c increases. The curves for the base case and the second case of $\Delta\Delta G_i = 0$ are indistinguishable, while the curve for the third case of $\chi_i = 0$ is markedly suppressed. This indicates that $\Delta\Delta G_i$ is unimportant here and the cation size effect is mainly ascribed to the surface charging effects. The surface charging relation for the third case of $\chi_i = 0$ is shown in Figure 6b. Compared with Figure 2d for the base case, Figure 6b exhibits a reduced difference of σ for different d_c's, thus leading to a much reduced d_c-dependence of the OER current in Figure 6a. In addition, compared with the base case, σ has a smaller magnitude for $\chi_i = 0$, because negatively charged adsorbates increase the pzc of the electrode.[66] As a result, the cation overcrowding effect is diminished for the third case of $\chi_i = 0$.

Our argument that the cation effect on the OER is mainly caused by surface charging effects instead of the shift in the field-dependent binding energies is further supported by the results presented in Figure 6c. The x-axis is the potential of zero charge which dictates the surface charging relation. The y-axis is the serial number of Monte Carlo simulations in which $U_1^{\ominus}$, $U_2^{\ominus}$, $U_3^{\ominus}$ are allowed to vary randomly within 0.2 V around their base values. U_4 is given by the constraint condition that $U_4^{\ominus} = 4.92 - U_1^{\ominus} - U_2^{\ominus} - U_4^{\ominus}$. It is clearly shown that the OER current ratio between Cs^+ and Li^+ at 1.7 V_{SHE}, $\frac{j_{1.7V_{RHE}}(Cs^+)}{j_{1.7V_{RHE}}(Li^+)}$, increases significantly when the pzc grows, namely, when the electrode surface gets more negatively charged. On the contrary, $\frac{j_{1.7V_{RHE}}(Cs^+)}{j_{1.7V_{RHE}}(Li^+)}$ is slightly affected by random variations in the equilibrium potentials of the elementary steps which are determined by the binding energies of the adsorbates. The insensitivity of the cation effects to binding energies is in accord with the robustness of the cation effects observed in a wide range of catalysts in experiments, including Ni(Fe)OOH, RuO_2, Au, IrO_2, and perovskites.[14,24−26,28]

Continuing in our line of reasoning, we deduce that the effect of cation size will be less significant for catalysts with a lower pzc. Titanium dioxide (TiO_2) has a work function of 5.4 eV, around 1 eV lower than that of nickel oxides. Based on the linear relation between the work function and the pzc, TiO_2 shall carry a positive charge on its surface during the OER. Therefore, if electrostatic factors, more precisely, the surface-charge modulated cation overcrowding effects, dominate, we expect that the cation size effect on the OER is much weaker at TiO_2 compared with NiO. A systematic comparison of the cation effects on different catalysts with different work functions is vital to examine the importance of surface charging effects in the cation effects on the OER.

Parameter Sensitivity and Robustness of the Model Results

Given the significant number of parameters in our model, we shall dissect the robustness of the model results against uncertainties and variations in model parameters. To this end, a parameter sensitivity study is conducted. Among model parameters in Table 1, those having significant uncertainties and variations include the pzc, the equilibrium potentials $U_i^{\ominus}$ (equivalently, the binding energies), the activation barriers $G_{a,i}^{\ominus}$, the transfer coefficients (β_i), and the net charge numbers of adsorbed intermediates ξ_i. In the preceding subsection, we have shown that the cation effects are highly sensitive to the pzc and robust against variations in $U_i^{\ominus}$. In this subsection, we complement the parametric analysis by examining the influence of $G_{a,i}^{\ominus}$, ξ_i, and β_i. The output of the model used for the sensitivity analysis is the current density ratio between Cs^+ and Li^+ at 1.7 V_{RHE}, denoted as $\frac{j_{1.7V_{RHE}}(Cs^+)}{j_{1.7V_{RHE}}(Li^+)}$. Three groups of Monte Carlo simulations were conducted. Each group consists of 100 runs of the model. In each run, the four $G_{a,i}^{\ominus}$'s are varied randomly in the range of [0.3, 0.6] eV in the first group, the four ξ_i's are varied randomly in the range of [−0.1, 0] in the second group, and β_i is changed randomly in the range of [0.3, 0.7] in the third group.

The histogram of the Monte Carlo simulation is exhibited in Figure 7. All data points of $\frac{j_{1.7V_{RHE}}(Cs^+)}{j_{1.7V_{RHE}}(Li^+)}$ in the first group are above 2, indicating that the trend of higher OER activity at smaller d_c is robust against variations in $G_{a,i}^{\ominus}$'s. The data points in the second group are more dispersed, indicating that $\frac{j_{1.7V_{RHE}}(Cs^+)}{j_{1.7V_{RHE}}(Li^+)}$ is highly sensitive to the four ξ_i's because they determine the surface charging relation and thus the cation overcrowding phenomenon, as has been analyzed for the third case in Figure 6a. This gives further evidence to our claim in the preceding subsection that alkali metal cations influence the OER activity mainly by modulating the local reaction conditions determined by the surface charge density. The distribution of data points in the third group is much smaller, indicating that $\frac{j_{1.7V_{RHE}}(Cs^+)}{j_{1.7V_{RHE}}(Li^+)}$ is less sensitive to the transfer coefficients.

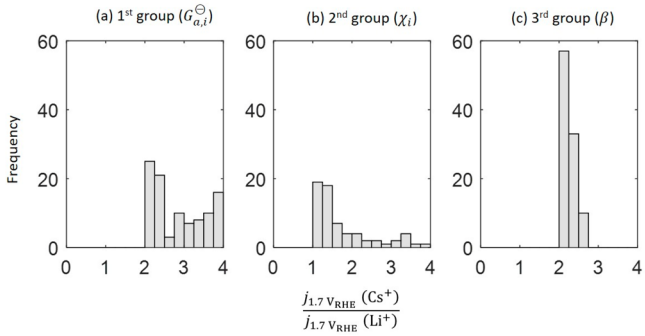

Figure 7. Histogram of the Monte Carlo simulation. The horizontal axis is the current density ratio between Cs^+ and Li^+ at 1.7 V_{RHE}. Three groups of Monte Carlo simulation were conducted. Each group consists of 100 runs of the model. In each run, the four $G_{a,i}^{\ominus}$'s are varied randomly in the range of [0.3, 0.6] eV in the first group, the four ξ_i's are varied randomly in the range of [−0.1, 0] in the second group, and the transfer coefficient β_i is varied randomly in the range of [0.3, 0.7]. Other parameters have their base values as listed in Table 1.

Features, Limitations, and Extensions

In this subsection, we first dissect the features of the presented model compared with existing models. Then, we address the question: to what extent are the insights presented here valid for other cases. This requires us to scrutinize assumptions and limitations of the model. Afterward, we discuss modifications and extensions needed to implant the model for more general cases.

Taking a broader view, combining DFT calculations and microkinetic considerations in modeling electrocatalytic reactions is becoming increasingly popular.[30,31,81] Some studies

https://doi.org/10.1021/jacsau.1c00315
JACS Au 2021, 1, 1752−1765

have used mean-field EDL models to compute the local reaction condition for the ORR[29,82,83] and carbon dioxide reduction.[33,76] As for the OER, our model is, to the best of our knowledge, the first one that combines DFT calculations, microkinetic considerations, and an EDL model. Moreover, compared with similar models that were developed for other reactions,[33,76,81,82] this model has two unique features. First, the EDL model considers nonlinear solvent polarization and ion size effect. Second, chemisorption-induced surface dipoles, significantly influencing the surface charging relation, are considered.

The assumptions and approximations of the model are fivefold. First, the microkinetic model is developed based on the OER mechanism consisting of four OH^--coupled electron transfer steps expressed in eqs 14−17. Second, the phenomenological Butler−Volmer equation is used to describe electron transfer kinetics. Third, the EDL is considered as a serial connection of a charged adlayer and a diffuse layer and treated at the mean field level for the one-dimensional case. Fourth, the electrolyte cations are restricted to be nonspecifically adsorbed. Fifth, macroscopic mass transport effects are neglected.

On the first point, the used reaction mechanism is common to many OER catalysts, though the active sites, the binding energies, and the activation energies are case-specific. We have demonstrated in the preceding subsection that our results are robust against variations in these parameters. For OER catalysts with decoupled OH^- and electron transfer steps, the microkinetic model can be modified without major difficulties.

On the second point, the Butler−Volmer equation can be upgraded to more advanced electron transfer theories, however, at the cost of introducing additional microscopic parameters. For example, the Marcus−Hush−Chidsey theory requires the knowledge of interfacial solvent reorganization energies, and the Anderson−Newns model requires the knowledge of electronic interactions between the catalyst and the reactant in solution. Therefore, the Butler−Volmer equation best suits our purpose. In addition, the Marcus−Hush−Chidsey theory can be reduced to the Butler−Volmer equation with a potential-dependent transfer coefficient. Our sensitivity analysis shows that variations in the transfer coefficient do not alter the conclusion.

On the third point, the mean-field EDL model radically simplifies the atomistic picture of the EDL which can be obtained from DFT-based first-principles calculations.[84,85] Atomistic EDL models, such as in refs 86 and 87, can complement the mean-field EDL model by determining some of the model parameters, including the structure of the adlayer and the net charge numbers of adsorbed intermediates. We are aware that the ξ_i's are difficult to obtain accurately and depend on the theoretical method used. Through sensitivity analysis, we have shown that the cation effects are highly sensitive to ξ_i's.

On the fourth point, there is a controversy around whether electrolyte cations are nonspecifically adsorbed,[28,88] specifically adsorbed,[26,89] or even intercalated into the electrode material.[25] As for alkali metal cations at a NiOOH surface, Garcia et al. showed that the electrochemical active surface area (ECSA) is not influenced significantly by electrolyte cations,[14] invalidating a previous postulate that the cation-dependent activity is related to the ECSA change due to cation intercalation.[25] The crystal truncation rod analysis of Rao et al. indicates that Li^+ and K^+ are nonspecifically adsorbed and retain their solvation shells near the RuO_2 surface.[28] This provides experimental evidence for the assumption of nonspecific adsorption in this model. For the case with specific adsorption of cations, its effect usually translates to a shift in binding energies.[14,26] For such cases, we recall that the findings of the present model are robust against variations in binding energies, prompting us to conclude that the present model would remain applicable for the case of specific adsorption of cations.

On the fifth point, mass transport is one of the influencing factors of the polarization curves, and its importance is crucial in the high overpotential region where the current density is rather high. The presented study focused on the cation effect on the intrinsic catalytic activity in the low overpotential region. Therefore, the mass transport effects are secondary in this work. A comprehensive physicochemical model for electrocatalytic reactions considering multistep interfacial kinetics, EDL effects, and macroscopic mass transport effects has been developed recently.[90]

CONCLUSION

We have presented a physicochemical model for understanding how electrolyte cations influence the OER via shaping the local reaction conditions. The decreasing OER activity with larger cations was found to be correlated with cation overcrowding effects in the electric double layer. Specifically, the electrode surface is negatively charged due to the high pzc, resulting in cation accumulation and anion depletion near the electrode. Furthermore, cations with larger effective size occupy more volume, leading to smaller concentrations of OH^- and thus lower OER activity. The same reasoning has been employed to understand why the OER activity increases with solution pH on the RHE scale and why the OER activity decreases in the presence of bivalent cations. The correction to the binding energies that depend on the local electric field plays a minor role in our case. A sensitivity analysis shows that the cation size effect is sensitive to properties related to the surface charging behavior, including the potential of zero charge and the net charge numbers of adsorbed intermediates. In addition, Monte Carlo simulations demonstrated that the key findings reported are robust against uncertainties and variations in binding energies, activation barriers, and transfer coefficients. This work adds to the understanding of how the local reaction environment influences electrocatalytic activities.

ASSOCIATED CONTENT

Supporting Information

The Supporting Information is available free of charge at https://pubs.acs.org/doi/10.1021/jacsau.1c00315.

Model fitting details; results for an extreme case with one step having a much larger activation energy; zero-point vibrational corrections; projected magnetic moments for oxygen and nickel atoms; variations in experimental polarization curves on the same system measured by different laboratories (PDF)

AUTHOR INFORMATION

Corresponding Author

Jun Huang − *Institute of Theoretical Chemistry, Ulm University, 89069 Ulm, Germany; Institute of Energy and Climate Research, IEK-13: Theory and Computation of*

https://doi.org/10.1021/jacsau.1c00315
JACS Au 2021, 1, 1752−1765

Energy Materials, Forschungszentrum Jülich GmbH, 52425 Jülich, Germany; orcid.org/0000-0002-1668-5361; Email: jun.huang@uni-ulm.de

Authors

Mengru Li − *Institute of Theoretical Chemistry, Ulm University, 89069 Ulm, Germany*

Mohammad J. Eslamibidgoli − *Institute of Energy and Climate Research, IEK-13: Theory and Computation of Energy Materials, Forschungszentrum Jülich GmbH, 52425 Jülich, Germany*

Michael Eikerling − *Institute of Energy and Climate Research, IEK-13: Theory and Computation of Energy Materials, Forschungszentrum Jülich GmbH, 52425 Jülich, Germany; Jülich Aachen Research Alliance: JARA-Energy, 52425 Jülich, Germany;* orcid.org/0000-0002-0764-8948

Axel Groß − *Institute of Theoretical Chemistry, Ulm University, 89069 Ulm, Germany; Helmholtz Institute Ulm (HIU) Electrochemical Energy Storage, 89069 Ulm, Germany;* orcid.org/0000-0003-4037-7331

Complete contact information is available at: https://pubs.acs.org/10.1021/jacsau.1c00315

Author Contributions

J.H.: conceptualization, investigation, writing—original draft. M.L.: DFT calculations, writing—review and editing. M.J. E.: DFT calculations, writing—review and editing. M.E.: writing—review and editing, supervision. A.G.: writing—review and editing, supervision.

Notes

The authors declare no competing financial interest.

■ ACKNOWLEDGMENTS

J.H. acknowledges the financial support from the Alexander von Humboldt Foundation and National Natural Science Foundation of China under Grant Number of 21802170. M.E. acknowledges the financial support from Forschungszentrum Jülich GmbH. Computer time provided by the state of Baden-Württemberg through bwHPC and the German Research Foundation (DFG) through Grant No. INST 40/575-1 FUGG (JUSTUS 2 cluster) is gratefully acknowledged. This work contributes to the research performed at CELEST (Center for Electrochemical Energy Storage Ulm-Karlsruhe).

■ REFERENCES

(1) Nørskov, J. K.; Bligaard, T.; Logadottir, A.; Kitchin, J. R.; Chen, J. G.; Pandelov, S.; Stimming, U. Trends in the Exchange Current for Hydrogen Evolution. *J. Electrochem. Soc.* **2005**, *152* (3), J23.

(2) Quaino, P.; Juarez, F.; Santos, E.; Schmickler, W. Volcano plots in hydrogen electrocatalysis − uses and abuses. *Beilstein J. Nanotechnol.* **2014**, *5*, 846−854.

(3) Schmickler, W. On the Theory of Electrocatalysis. In *Electrochemical Science for a Sustainable Society: A Tribute to John O'M Bockris*; Uosaki, K., Ed.; Springer International Publishing: Cham, 2017; pp 95−111.

(4) Exner, K. S. Why approximating electrocatalytic activity by a single free-energy change is insufficient. *Electrochim. Acta* **2021**, *375*, 137975.

(5) Bandarenka, A. S.; Koper, M. T. M. Structural and electronic effects in heterogeneous electrocatalysis: Toward a rational design of electrocatalysts. *J. Catal.* **2013**, *308*, 11−24.

(6) Nørskov, J. K.; Bligaard, T.; Rossmeisl, J.; Christensen, C. H. Towards the computational design of solid catalysts. *Nat. Chem.* **2009**, *1* (1), 37−46.

(7) Strmcnik, D.; Kodama, K.; van der Vliet, D.; Greeley, J.; Stamenkovic, V. R.; Marković, N. M. The role of non-covalent interactions in electrocatalytic fuel-cell reactions on platinum. *Nat. Chem.* **2009**, *1* (6), 466−472.

(8) Xue, S.; Garlyyev, B.; Watzele, S.; Liang, Y.; Fichtner, J.; Pohl, M. D.; Bandarenka, A. S. Influence of Alkali Metal Cations on the Hydrogen Evolution Reaction Activity of Pt, Ir, Au, and Ag Electrodes in Alkaline Electrolytes. *ChemElectroChem* **2018**, *5* (17), 2326−2329.

(9) Liu, E.; Li, J.; Jiao, L.; Doan, H. T. T.; Liu, Z.; Zhao, Z.; Huang, Y.; Abraham, K. M.; Mukerjee, S.; Jia, Q. Unifying the Hydrogen Evolution and Oxidation Reactions Kinetics in Base by Identifying the Catalytic Roles of Hydroxyl-Water-Cation Adducts. *J. Am. Chem. Soc.* **2019**, *141* (7), 3232−3239.

(10) Waegele, M. M.; Gunathunge, C. M.; Li, J.; Li, X. How cations affect the electric double layer and the rates and selectivity of electrocatalytic processes. *J. Chem. Phys.* **2019**, *151* (16), 160902.

(11) Suntivich, J.; Perry, E. E.; Gasteiger, H. A.; Shao-Horn, Y. The Influence of the Cation on the Oxygen Reduction and Evolution Activities of Oxide Surfaces in Alkaline Electrolyte. *Electrocatalysis* **2013**, *4* (1), 49−55.

(12) Tymoczko, J.; Colic, V.; Ganassin, A.; Schuhmann, W.; Bandarenka, A. S. Influence of the alkali metal cations on the activity of Pt(111) towards model electrocatalytic reactions in acidic sulfuric media. *Catal. Today* **2015**, *244*, 96−102.

(13) Zhu, S.; Hu, X.; Zhang, L.; Shao, M. Impacts of Perchloric Acid, Nafion, and Alkali Metal Ions on Oxygen Reduction Reaction Kinetics in Acidic and Alkaline Solutions. *J. Phys. Chem. C* **2016**, *120* (48), 27452−27461.

(14) Garcia, A. C.; Touzalin, T.; Nieuwland, C.; Perini, N.; Koper, M. T. M. Enhancement of Oxygen Evolution Activity of Nickel Oxyhydroxide by Electrolyte Alkali Cations. *Angew. Chem., Int. Ed.* **2019**, *58* (37), 12999−13003.

(15) Sakong, S.; Groß, A. The Importance of the Electrochemical Environment in the Electro-Oxidation of Methanol on Pt(111). *ACS Catal.* **2016**, *6* (8), 5575−5586.

(16) Resasco, J.; Chen, L. D.; Clark, E.; Tsai, C.; Hahn, C.; Jaramillo, T. F.; Chan, K.; Bell, A. T. Promoter Effects of Alkali Metal Cations on the Electrochemical Reduction of Carbon Dioxide. *J. Am. Chem. Soc.* **2017**, *139* (32), 11277−11287.

(17) Ludwig, T.; Gauthier, J. A.; Dickens, C. F.; Brown, K. S.; Ringe, S.; Chan, K.; Nørskov, J. K. Atomistic Insight into Cation Effects on Binding Energies in Cu-Catalyzed Carbon Dioxide Reduction. *J. Phys. Chem. C* **2020**, *124* (45), 24765−24775.

(18) Erdey-Grúz, T.; Shafarik, I. In *Soviet Electrochemistry*; Proceedings of the 4th Conference on Electrochemistry; Consultants Bureau, New York: 1961; p 145.

(19) Kozawa, A. Effects of anions and cations on oxygen reduction and oxygen evolution reactions on platinum electrodes. *J. Electroanal. Chem. (1959-1966)* **1964**, *8* (1), 20−39.

(20) Armstrong, R. A.; Briggs, G. W. D.; Moore, M. A. The effect of lithium in preventing iron poisoning in the nickel hydroxide electrode. *Electrochim. Acta* **1986**, *31* (1), 25−27.

(21) Uñates, M. E.; Folquer, M. E.; Vilche, J. R.; Arvia, A. J. The Influence of Foreign Cations on the Electrochemical Behavior of the Nickel Hydroxide Electrode. *J. Electrochem. Soc.* **1992**, *139* (10), 2697−2704.

(22) Barnard, R.; Randell, C. F.; Tye, F. L. Studies concerning charged nickel hydroxide electrodes IV. Reversible potentials in LiOH, NaOH, RbOH and CsOH. *J. Appl. Electrochem.* **1981**, *11* (4), 517−523.

(23) Vishnu Kamath, P.; Ahmed, M. F. Cyclic voltammetric studies of nickel hydroxide and cobalt hydroxide thin films in alkali and alkaline earth metal hydroxides. *J. Appl. Electrochem.* **1993**, *23* (3), 225−230.

(24) Michael, J. D.; Demeter, E. L.; Illes, S. M.; Fan, Q.; Boes, J. R.; Kitchin, J. R. Alkaline Electrolyte and Fe Impurity Effects on the

Performance and Active-Phase Structure of NiOOH Thin Films for OER Catalysis Applications. *J. Phys. Chem. C* **2015**, *119* (21), 11475−11481.
(25) Zaffran, J.; Stevens, M. B.; Trang, C. D. M.; Nagli, M.; Shehadeh, M.; Boettcher, S. W.; Caspary Toroker, M. Influence of Electrolyte Cations on Ni(Fe)OOH Catalyzed Oxygen Evolution Reaction. *Chem. Mater.* **2017**, *29* (11), 4761−4767.
(26) Yang, C.; Fontaine, O.; Tarascon, J.-M.; Grimaud, A. Chemical Recognition of Active Oxygen Species on the Surface of Oxygen Evolution Reaction Electrocatalysts. *Angew. Chem., Int. Ed.* **2017**, *56* (30), 8652−8656.
(27) Perini, N.; Ticianelli, E. A. Oxygen evolution on gold: The effects of alkali-metal cations and iron impurities from alkaline electrolytes. *J. Catal.* **2019**, *378*, 277−282.
(28) Rao, R. R.; Huang, B.; Katayama, Y.; Hwang, J.; Kawaguchi, T.; Lunger, J. R.; Peng, J.; Zhang, Y.; Morinaga, A.; Zhou, H.; You, H.; Shao-Horn, Y. pH- and Cation-Dependent Water Oxidation on Rutile RuO2(110). *J. Phys. Chem. C* **2021**, *125* (15), 8195−8207.
(29) Huang, J.; Zhang, J.; Eikerling, M. Unifying theoretical framework for deciphering the oxygen reduction reaction on platinum. *Phys. Chem. Chem. Phys.* **2018**, *20* (17), 11776−11786.
(30) Dickens, C. F.; Kirk, C.; Nørskov, J. K. Insights into the Electrochemical Oxygen Evolution Reaction with ab Initio Calculations and Microkinetic Modeling: Beyond the Limiting Potential Volcano. *J. Phys. Chem. C* **2019**, *123* (31), 18960−18977.
(31) Govind Rajan, A.; Carter, E. A. Microkinetic model for pH- and potential-dependent oxygen evolution during water splitting on Fe-doped *β*-NiOOH. *Energy Environ. Sci.* **2020**, *13* (12), 4962−4976.
(32) Sinha, V.; Sun, D.; Meijer, E. J.; Vlugt, T. J. H.; Bieberle-Hütter, A. A multiscale modelling approach to elucidate the mechanism of the oxygen evolution reaction at the hematite−water interface. *Faraday Discuss.* **2021**, *229* (229), 89−107.
(33) Ringe, S.; Morales-Guio, C. G.; Chen, L. D.; Fields, M.; Jaramillo, T. F.; Hahn, C.; Chan, K. Double layer charging driven carbon dioxide adsorption limits the rate of electrochemical carbon dioxide reduction on Gold. *Nat. Commun.* **2020**, *11* (1), 33.
(34) Zhang, M.-K.; Wei, Z.; Chen, W.; Xu, M.-L.; Cai, J.; Chen, Y.-X. Bell shape vs volcano shape pH dependent kinetics of the electrochemical oxidation of formic acid and formate, intrinsic kinetics or local pH shift? *Electrochim. Acta* **2020**, *363*, 137160.
(35) Zhang, M.-K.; Chen, W.; Wei, Z.; Xu, M.-L.; He, Z.; Cai, J.; Chen, Y.-X.; Santos, E. Mechanistic Implication of the pH Effect and H/D Kinetic Isotope Effect on HCOOH/HCOO− Oxidation at Pt Electrodes: A Study by Computer Simulation. *ACS Catal.* **2021**, *11*, 6920−6930.
(36) Blöchl, P. E. Projector augmented-wave method. *Phys. Rev. B: Condens. Matter Mater. Phys.* **1994**, *50* (24), 17953−17979.
(37) Kresse, G.; Joubert, D. From ultrasoft pseudopotentials to the projector augmented-wave method. *Phys. Rev. B: Condens. Matter Mater. Phys.* **1999**, *59* (3), 1758−1775.
(38) Kresse, G.; Furthmüller, J. Efficient iterative schemes for ab initio total-energy calculations using a plane-wave basis set. *Phys. Rev. B: Condens. Matter Mater. Phys.* **1996**, *54* (16), 11169−11186.
(39) Kresse, G.; Furthmüller, J. Efficiency of ab-initio total energy calculations for metals and semiconductors using a plane-wave basis set. *Comput. Mater. Sci.* **1996**, *6* (1), 15−50.
(40) Kresse, G.; Hafner, J. Ab initio molecular-dynamics simulation of the liquid-metal–amorphous-semiconductor transition in germanium. *Phys. Rev. B: Condens. Matter Mater. Phys.* **1994**, *49* (20), 14251−14269.
(41) Perdew, J. P.; Burke, K.; Ernzerhof, M. Generalized Gradient Approximation Made Simple. *Phys. Rev. Lett.* **1996**, *77* (18), 3865−3868.
(42) Dudarev, S. L.; Botton, G. A.; Savrasov, S. Y.; Humphreys, C. J.; Sutton, A. P. Electron-energy-loss spectra and the structural stability of nickel oxide: An LSDA+U study. *Phys. Rev. B: Condens. Matter Mater. Phys.* **1998**, *57* (3), 1505−1509.
(43) Wang, L.; Maxisch, T.; Ceder, G. Oxidation energies of transition metal oxides within the $\mathrm{GGA}+\mathrm{U}$ framework. *Phys. Rev. B: Condens. Matter Mater. Phys.* **2006**, *73* (19), 195107.
(44) Eslamibidgoli, M. J.; Groß, A.; Eikerling, M. Surface configuration and wettability of nickel(oxy)hydroxides: a first-principles investigation. *Phys. Chem. Chem. Phys.* **2017**, *19* (34), 22659−22669.
(45) Li, Y.-F.; Selloni, A. Mechanism and Activity of Water Oxidation on Selected Surfaces of Pure and Fe-Doped NiOx. *ACS Catal.* **2014**, *4* (4), 1148−1153.
(46) Grimme, S.; Ehrlich, S.; Goerigk, L. Effect of the damping function in dispersion corrected density functional theory. *J. Comput. Chem.* **2011**, *32* (7), 1456−1465.
(47) Reuter, K.; Frenkel, D.; Scheffler, M. The Steady State of Heterogeneous Catalysis, Studied by First-Principles Statistical Mechanics. *Phys. Rev. Lett.* **2004**, *93* (11), 116105.
(48) Reuter, K.; Scheffler, M. First-principles kinetic Monte Carlo simulations for heterogeneous catalysis: Application to the CO oxidation at $\mathrm{Ru}{\mathrm{O}}_{2}(110)$. *Phys. Rev. B: Condens. Matter Mater. Phys.* **2006**, *73* (4), 045433.
(49) Nørskov, J. K.; Rossmeisl, J.; Logadottir, A.; Lindqvist, L.; Kitchin, J. R.; Bligaard, T.; Jónsson, H. Origin of the Overpotential for Oxygen Reduction at a Fuel-Cell Cathode. *J. Phys. Chem. B* **2004**, *108* (46), 17886−17892.
(50) Groß, A. Grand-canonical approaches to understand structures and processes at electrochemical interfaces from an atomistic perspective. *Current Opinion in Electrochemistry* **2021**, *27*, 100684.
(51) Diaz-Morales, O.; Ferrus-Suspedra, D.; Koper, M. T. M. The importance of nickel oxyhydroxide deprotonation on its activity towards electrochemical water oxidation. *Chemical Science* **2016**, *7* (4), 2639−2645.
(52) Lee, S.; Banjac, K.; Lingenfelder, M.; Hu, X. Oxygen Isotope Labeling Experiments Reveal Different Reaction Sites for the Oxygen Evolution Reaction on Nickel and Nickel Iron Oxides. *Angew. Chem., Int. Ed.* **2019**, *58* (30), 10295−10299.
(53) Linstrom, P. J.; Mallard, W. G. The NIST Chemistry WebBook: A chemical data resource on the internet. *J. Chem. Eng. Data* **2001**, *46* (5), 1059−1063.
(54) Govind Rajan, A.; Martirez, J. M. P.; Carter, E. A. Facet-Independent Oxygen Evolution Activity of Pure *β*-NiOOH: Different Chemistries Leading to Similar Overpotentials. *J. Am. Chem. Soc.* **2020**, *142* (7), 3600−3612.
(55) Rossmeisl, J.; Qu, Z. W.; Zhu, H.; Kroes, G. J.; Nørskov, J. K. Electrolysis of water on oxide surfaces. *J. Electroanal. Chem.* **2007**, *607* (1), 83−89.
(56) Man, I. C.; Su, H.-Y.; Calle-Vallejo, F.; Hansen, H. A.; Martínez, J. I.; Inoglu, N. G.; Kitchin, J.; Jaramillo, T. F.; Nørskov, J. K.; Rossmeisl, J. Universality in Oxygen Evolution Electrocatalysis on Oxide Surfaces. *ChemCatChem* **2011**, *3* (7), 1159−1165.
(57) Divanis, S.; Kutlusoy, T.; Ingmer Boye, I. M.; Man, I. C.; Rossmeisl, J. Oxygen evolution reaction: a perspective on a decade of atomic scale simulations. *Chemical Science* **2020**, *11* (11), 2943−2950.
(58) Bajpai, A.; Frey, K.; Schneider, W. F. Comparison of Coverage-Dependent Binding Energy Models for Mean-Field Microkinetic Rate Predictions. *Langmuir* **2020**, *36* (1), 465−474.
(59) Chen, L. D.; Urushihara, M.; Chan, K.; Nørskov, J. K. Electric Field Effects in Electrochemical CO2 Reduction. *ACS Catal.* **2016**, *6* (10), 7133−7139.
(60) Sandberg, R. B.; Montoya, J. H.; Chan, K.; Nørskov, J. K. CO-CO coupling on Cu facets: Coverage, strain and field effects. *Surf. Sci.* **2016**, *654*, 56−62.
(61) Huang, J. Hybrid Density-Potential Functional Theory of Electric Double Layers. *Electrochim. Acta* **2021**, *389*, 138720.
(62) Huang, J.; Chen, S.; Eikerling, M. Grand-Canonical Model of Electrochemical Double Layers from a Hybrid Density−Potential Functional. *J. Chem. Theory Comput.* **2021**, *17* (4), 2417−2430.
(63) Abrashkin, A.; Andelman, D.; Orland, H. Dipolar Poisson-Boltzmann Equation: Ions and Dipoles Close to Charge Interfaces. *Phys. Rev. Lett.* **2007**, *99* (7), 077801.

https://doi.org/10.1021/jacsau.1c00315
JACS Au 2021, 1, 1752−1765

(64) Gongadze, E.; Iglič, A. Decrease of permittivity of an electrolyte solution near a charged surface due to saturation and excluded volume effects. *Bioelectrochemistry* **2012**, *87*, 199−203.
(65) Zhang, Y.; Huang, J. Treatment of Ion-Size Asymmetry in Lattice-Gas Models for Electrical Double Layer. *J. Phys. Chem. C* **2018**, *122* (50), 28652−28664.
(66) Huang, J.; Malek, A.; Zhang, J.; Eikerling, M. H. Non-monotonic Surface Charging Behavior of Platinum: A Paradigm Change. *J. Phys. Chem. C* **2016**, *120* (25), 13587−13595.
(67) Huang, J.; Zhou, T.; Zhang, J.; Eikerling, M. Double layer of platinum electrodes: Non-monotonic surface charging phenomena and negative double layer capacitance. *J. Chem. Phys.* **2018**, *148* (4), 044704.
(68) Israelachvili, J. N. *Intermolecular and surface forces*; Academic Press: 2015.
(69) Wellendorff, J.; Silbaugh, T. L.; Garcia-Pintos, D.; Nørskov, J. K.; Bligaard, T.; Studt, F.; Campbell, C. T. A benchmark database for adsorption bond energies to transition metal surfaces and comparison to selected DFT functionals. *Surf. Sci.* **2015**, *640*, 36−44.
(70) Huang, J. Mixed quantum-classical treatment of electron transfer at electrocatalytic interfaces: Theoretical framework and conceptual analysis. *J. Chem. Phys.* **2020**, *153* (16), 164707.
(71) Guidelli, R.; Compton, R. G.; Feliu, J. M.; Gileadi, E.; Lipkowski, J.; Schmickler, W.; Trasatti, S. Defining the transfer coefficient in electrochemistry: An assessment (IUPAC Technical Report). *Pure Appl. Chem.* **2014**, *86* (2), 245−258.
(72) Henkelman, G.; Uberuaga, B. P.; Jónsson, H. A climbing image nudged elastic band method for finding saddle points and minimum energy paths. *J. Chem. Phys.* **2000**, *113* (22), 9901−9904.
(73) Kosmulski, M. Isoelectric points and points of zero charge of metal (hydr)oxides: 50years after Parks' review. *Adv. Colloid Interface Sci.* **2016**, *238*, 1−61.
(74) Nakayama, Y.; Andelman, D. Differential capacitance of the electric double layer: The interplay between ion finite size and dielectric decrement. *J. Chem. Phys.* **2015**, *142* (4), 044706.
(75) Borukhov, I.; Andelman, D.; Orland, H. Steric Effects in Electrolytes: A Modified Poisson-Boltzmann Equation. *Phys. Rev. Lett.* **1997**, *79* (3), 435−438.
(76) Ringe, S.; Clark, E. L.; Resasco, J.; Walton, A.; Seger, B.; Bell, A. T.; Chan, K. Understanding cation effects in electrochemical CO2 reduction. *Energy Environ. Sci.* **2019**, *12* (10), 3001−3014.
(77) Koper, M. T. M. Theory of multiple proton−electron transfer reactions and its implications for electrocatalysis. *Chemical Science* **2013**, *4* (7), 2710−2723.
(78) Giordano, L.; Han, B.; Risch, M.; Hong, W. T.; Rao, R. R.; Stoerzinger, K. A.; Shao-Horn, Y. pH dependence of OER activity of oxides: Current and future perspectives. *Catal. Today* **2016**, *262*, 2−10.
(79) Grimaud, A.; Diaz-Morales, O.; Han, B.; Hong, W. T.; Lee, Y.-L.; Giordano, L.; Stoerzinger, K. A.; Koper, M. T. M.; Shao-Horn, Y. Activating lattice oxygen redox reactions in metal oxides to catalyse oxygen evolution. *Nat. Chem.* **2017**, *9* (5), 457−465.
(80) Duan, Y.; Dubouis, N.; Huang, J.; Dalla Corte, D. A.; Pimenta, V.; Xu, Z. J.; Grimaud, A. Revealing the Impact of Electrolyte Composition for Co-Based Water Oxidation Catalysts by the Study of Reaction Kinetics Parameters. *ACS Catal.* **2020**, *10* (7), 4160−4170.
(81) Huang, J.; Eikerling, M. Modeling the oxygen reduction reaction at platinum-based catalysts: A brief review of recent developments. *Current Opinion in Electrochemistry* **2019**, *13*, 157−165.
(82) Zhou, D.; Wei, J.; He, Z.-D.; Xu, M.-L.; Chen, Y.-X.; Huang, J. Combining Single Crystal Experiments and Microkinetic Modeling in Disentangling Thermodynamic, Kinetic, and Double-Layer Factors Influencing Oxygen Reduction. *J. Phys. Chem. C* **2020**, *124* (25), 13672−13678.
(83) Kelly, S. R.; Kirk, C.; Chan, K.; Nørskov, J. K. Electric Field Effects in Oxygen Reduction Kinetics: Rationalizing pH Dependence at the Pt(111), Au(111), and Au(100) Electrodes. *J. Phys. Chem. C* **2020**, *124* (27), 14581−14591.
(84) Abidi, N.; Lim, K. R. G.; Seh, Z. W.; Steinmann, S. N. Atomistic modeling of electrocatalysis: Are we there yet? *Wiley Interdiscip. Rev.: Comput. Mol. Sci.* **2021**, *11* (3), e1499.
(85) Magnussen, O. M.; Groß, A. Toward an Atomic-Scale Understanding of Electrochemical Interface Structure and Dynamics. *J. Am. Chem. Soc.* **2019**, *141* (12), 4777−4790.
(86) Sakong, S.; Groß, A. The electric double layer at metal-water interfaces revisited based on a charge polarization scheme. *J. Chem. Phys.* **2018**, *149* (8), 084705.
(87) Sakong, S.; Groß, A. Water structures on a Pt(111) electrode from ab initio molecular dynamic simulations for a variety of electrochemical conditions. *Phys. Chem. Chem. Phys.* **2020**, *22* (19), 10431−10437.
(88) Strmcnik, D.; van der Vliet, D. F.; Chang, K. C.; Komanicky, V.; Kodama, K.; You, H.; Stamenkovic, V. R.; Marković, N. M. Effects of Li+, K+, and Ba2+ Cations on the ORR at Model and High Surface Area Pt and Au Surfaces in Alkaline Solutions. *J. Phys. Chem. Lett.* **2011**, *2* (21), 2733−2736.
(89) Mills, J. N.; McCrum, I. T.; Janik, M. J. Alkali cation specific adsorption onto fcc(111) transition metal electrodes. *Phys. Chem. Chem. Phys.* **2014**, *16* (27), 13699−13707.
(90) Zhang, L.; Cai, J.; Chen, Y.; Huang, J. Modelling electrocatalytic reactions with a concerted treatment of multistep electron transfer kinetics and local reaction conditions. *J. Phys.: Condens. Matter* **2021**, DOI: 10.1088/1361-648X/ac26fb.

https://doi.org/10.1021/jacsau.1c00315
JACS Au 2021, 1, 1752−1765